3-D UNSTEADY FLOW STRUCTURES AROUND RECTANGULAR COLUMN IN OPEN CHANNELS BY MEANS OF NON-LINEAR *k-ε* MODEL

Ichiro Kimura
Department of Environmental and Information Sciences, Yokkaichi University
1200 Kayo-cho, Yokkaichi 512-8512, Japan

Takashi Hosoda
Department of Civil Engineering, Kyoto University
Yoshida, Sakyo-ku, Kyoto 606-8501, Japan

ABSTRUCT

The unsteady flow structures induced by Karman vortices and horseshoe vortices around a rectangular column are examined using 3-D numerical computations. The non-linear *k-ε* model with the effect of the strain and rotation parameters is adopted as the turbulence model. Applicability of the turbulence model to the Karman vortex shedding in the 2-D flow field is firstly investigated through the comparison of the calculated results with the experimental ones conducted in the closed water section by Lyn (1992) and the model constants are adjusted. Then, the 3-D computations of unsteady flows in open channels are carried out focusing on the Karman vortex and the horseshoe vortex generated around a cylinder. Effects of the depth on the 3-D flow structures in open channels are also discussed through the comparison of the numerical results under the different conditions of water depth.

INTRODUCTION

It is well known that the complex flow structures induced by the Karman vortex and the horseshoe vortex can be observed around a bluff structure in rivers. The resistance to the flow and the local scour around a structure are closely related to such flows, and the prediction of the 3-D flow behavior is important for the design of river structures.

In this study, we apply the non-linear *k-ε* model to the flows past a rectangular column from the practical point of view. To resolve the excessive production of turbulent energy *k* at the impinging region, the effects of the strain and rotation parameters on the eddy viscosity are introduced in turbulence modeling. The authors have verified the applicability of non-linear *k-ε* model including the effect of strain and rotation parameters to the flow induced by the shear instability (Hosoda et al, 1997). Prior to the study on open channel flows, 2-D calculations of the flow field under the conditions of the laboratory test by Lyn (1992), which is conducted in closed water channel (Re=2.2×10^4), is firstly carried out to verify the applicability of the numerical model and to adjust the model constants. The different models (standard *k-ε* model and three types of non-linear *k-ε* model) are applied and the differences of the results are examined in detail. Then, the 3-D computations of the flow in a open channel are done focusing on the Karman vortex and the horseshoe vortex generated around a column. Effects of the depth on the flow are also shown through the examination of the numerical results with different flow depth.

2-D CALCULATIONS OF FLOWS PAST A COLUMN

The 2-D calculations of flows under the conditions of the laboratory tests by Lyn (1992) and Lyn et al. (1995) (Re=2.2×10^4) are firstly carried out to investigate the applicability of the non-linear *k-ε* model to the periodic flow field and to adjust the model constants.

Basic Equations

The basic equations are composed of the continuity equation, the momentum equations, and the *k-ε* equations described below:

[Continuity equation]

$$\frac{\partial U_i}{\partial x_i}=0 \tag{1}$$

[Momentum equation]

$$\frac{\partial U_i}{\partial t}+\frac{\partial U_j U_i}{\partial x_j}=g_i-\frac{1}{\rho}\frac{\partial p}{\partial x_i}+\frac{\partial -\overline{u_i u_j}}{\partial x_j}+\nu\frac{\partial^2 U_i}{\partial x_j^{\,2}} \tag{2}$$

[*k-ε* equations]

$$\frac{\partial k}{\partial t}+\frac{\partial k U_j}{\partial x_j}=-\overline{u_i u_j}\frac{\partial U_i}{\partial x_j}-\varepsilon+\frac{\partial}{\partial x_j}\left\{\left(\frac{D_t}{\sigma_k}+\nu\right)\frac{\partial k}{\partial x_j}\right\} \tag{3}$$

$$\frac{\partial \varepsilon}{\partial t}+\frac{\partial \varepsilon U_j}{\partial x_j}=-C_{\varepsilon 1}\overline{u_i u_j}\frac{\partial U_i}{\partial x_j}-C_{\varepsilon 2}\frac{\varepsilon^2}{k}+\frac{\partial}{\partial x_j}\left\{\left(\frac{D_t}{\sigma_\varepsilon}+\nu\right)\frac{\partial \varepsilon}{\partial x_j}\right\} \tag{4}$$

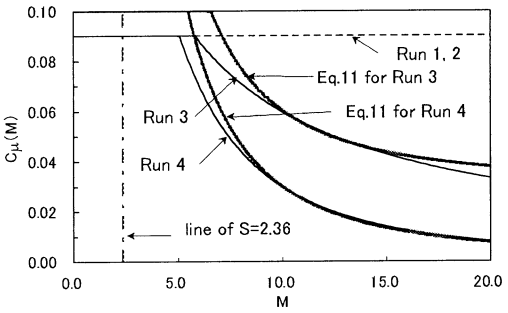

Figure 1. Relation between M and $C\mu$

where x_i : spatial coordinates, t : time, U_i: components of averaged velocity vectors, u_i : components of turbulent velocity vectors, p : averaged pressure, ρ: density of fluid, k : averaged turbulent energy, ε : averaged turbulent energy dissipation rate, D_t : eddy viscosity coefficient, ν: molecular dynamic viscosity coefficient, σ_k, σ_ε, $C_{\varepsilon 1}$, $C_{\varepsilon 2}$: model constants (σ_k=1.0, σ_ε=1.3, $C_{\varepsilon 1}$=1.44, $C_{\varepsilon 2}$=1.92 are used.).

Turbulence Modeling

The following four turbulence models were tested.

Run 1 (Standard k-ε model). The Reynolds stress tensors are evaluated by the following standard k-ε model.

$$-\overline{u_i u_j} = D_t S_{ij} - \frac{2}{3}k\delta_{ij}\ ,\quad S_{ij} = \frac{\partial U_i}{\partial x_j} + \frac{\partial U_j}{\partial x_i}, D_t = C_\mu \frac{k^2}{\varepsilon} \quad (5)$$

where $C\mu$ is a constant (=0.09). The standard k-ε model has the significant defect for the flows with impinging regions due to the excessive production of turbulence energy k (Kato and Launder, 1993).

Run 2. The quadratic non-linear terms of the constitutive equation are incorporated in Run 2. The Reynolds stress tensors are evaluated by the following equations (Yoshizawa, 1984), which are equivalent to the representation by Pope (1975) and by Gatski and Speziale (1993).

$$-\overline{u_i u_j} = D_t S_{ij} - \frac{2}{3}k\delta_{ij} - \frac{k}{\varepsilon}D_t \sum_{\beta=1}^{3} C_\beta \left(S_{\beta ij} - \frac{1}{3}S_{\beta\alpha\alpha}\delta_{ij} \right) \quad (6)$$

$$S_{1ij} = \frac{\partial U_i}{\partial x_r}\frac{\partial U_j}{\partial x_r}, S_{2ij} = \frac{1}{2}\left(\frac{\partial U_r}{\partial x_i}\frac{\partial U_j}{\partial x_r} + \frac{\partial U_r}{\partial x_j}\frac{\partial U_i}{\partial x_r} \right), S_{3ij} = \frac{\partial U_r}{\partial x_i}\frac{\partial U_r}{\partial x_j}$$

In Run 2, C_1=0.4, C_2=0, C_3=-0.13 and $C\mu$=0.09 are tested as model constants.

Run 3. Hosoda et al. (1997) reported that the vortices generated by the shear instability could not be reproduced numerically without including the effect of the strain parameter. In Run 3, the constants $C\mu$, C_1, C_2 and C_3 in Eq.(6) were replaced by the functions of strain parameter, S and rotation parameter, Ω.

$$C_\mu = \min\left(0.09, \frac{0.3}{1+0.4M}\right),\ C_1 = \frac{0.4}{1+0.01M^2},\ C_2 = 0,$$

$$C_3 = \frac{-0.13}{1+0.01M^2},\quad M = \max(S,\Omega) \quad (7)$$

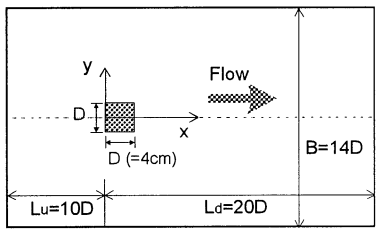

Figure 2. Computational flow domain

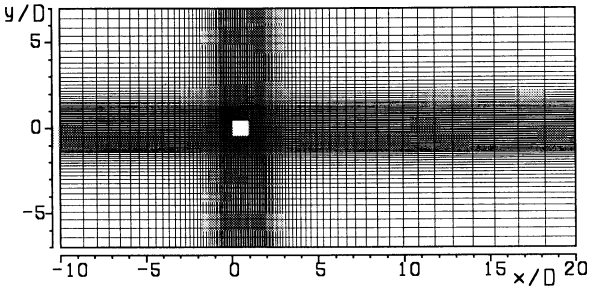

Figure 3. Numerical Grid

$$S = \frac{k}{\varepsilon}\sqrt{\frac{1}{2}\left(\frac{\partial U_i}{\partial x_j} + \frac{\partial U_j}{\partial x_i}\right)^2},\quad \Omega = \frac{k}{\varepsilon}\sqrt{\frac{1}{2}\left(\frac{\partial U_i}{\partial x_j} - \frac{\partial U_j}{\partial x_i}\right)^2} \quad (8)$$

Run 4. In Run 4, C_1(=0.4), C_2(=0) and C_3(=-0.13) in the non-linear terms are constants and $C\mu$ is set to be a function of S and Ω as follows.

$$C_\mu = \min\left(0.09, \frac{0.3}{1+0.09M^2}\right),\quad M = \max(S,\Omega) \quad (9)$$

Considerations of the Relation between $C\mu$ and M.

Some considerations about the relation between $C\mu$ and M in a simple shear flow, where all of the components of velocity gradients except $\partial U_1/\partial x_2$ are zero, are made. In a simple shear flow, since Ω=S or M=S, the relations between $C\mu$ and M in Run 3 and 4 are shown in Figure 1.

When the wall function method is applied as the wall boundary condition, the numerical value of M evaluated by the wall function is $1/\sqrt{2\times 0.09} \approx 2.36$. It is indicated that the non-linear k-ε models in Run 3 and 4 do not change the near wall boundary condition because $C\mu$ = 0.09 at $M \approx$ 2.36 in both the models.

The constraint for $C\mu$ itself can be derived from the condition of realizability.

$$\frac{\overline{u_2 u_2}}{k} = \frac{2}{3} + C_\mu \frac{2C_3 - C_1}{3}M^2\ ,\quad M = \frac{k}{\varepsilon}\left|\frac{\partial U_1}{\partial x_2}\right| \quad (10)$$

The condition of positive turbulent intensities requires the constraint denoted by Eq.(11).

$$C_\mu < \frac{2}{(C_1 - 2C_3)M^2} \quad (11)$$

The relations in Eq.(11) substituted by C_1 and C_3 in Run 3 and Run 4 are described in Figure 1. It is indicated that the realizability condition for a simple shear flow is satisfied in both the computations with Run 3 and Run 4.

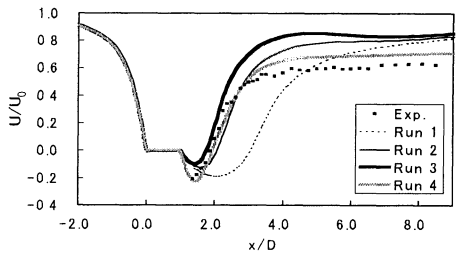

Figure 4. U/U_0 on x-axis

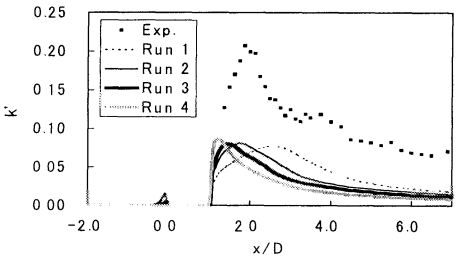

Figure 5. $k'=k/U_0^2$ on x-axis

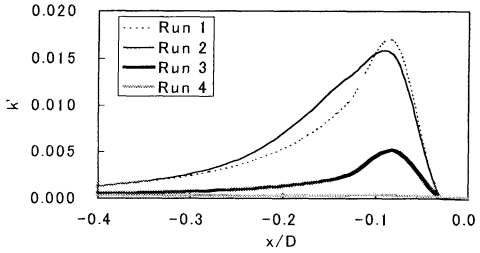

Figure 6. $k'=k/U_0^2$ on x-axis near the impinging region

Outline of Numerical Procedures

Descritization of the Basic Equations. The basic equations, (1)-(4) were discretized using the finite volume method in the staggered grid system. The QUICK scheme was applied to the convection terms and the central differencing was used for the diffusion terms in the momentum equations. The Hybrid central upwind scheme was applied to the k and ε equations. The Adams-Bashforth scheme with second-order accuracy in time was used for time integration of each equation. The basic equations were discretized as fully explicit forms and were solved successively along the time axis step by step. The pressure field was solved using iterative procedure at each time step.

Boundary and Initial Conditions. The flow domain in the calculation is shown in Figure 2.

The numerical grid used in the calculation is a variable rectangular one shown in Figure 3. The smallest distance of the grid lines near the column is 2mm ($=D/20$) and the maximum stretching of successive cells is limited to $0.9 \leqq q_x, q_y \leqq 1.1$, where $q_x = \Delta x_i/\Delta x_{i-1}$ and $q_y=\Delta y_j/\Delta y_{j-1}$. The number of the grid-points is 112 in x-direction and 92 in y-direction.

The wall functions were applied as the wall boundary conditions. At the down-stream end of the calculated domain, a zero stream-wise gradient was specified for velocities, k and ε. At the boundary inlet, the level of k was chosen to match the turbulence levels (= 2%) in the experiment by Lyn. The value of ε at the inlet was determined from the value of k at the inlet and Eq.(5) by specifying the ratio $Dt/\nu = 10$ (Bosche and Rodi, 1998).

At the beginning of the calculations, $U=U_0$=55cm/s, V=0, $k = k_{in}$ and $\varepsilon = \varepsilon_{in}$ (k_{in} and ε_{in} are the values of k and ε at the inlet boundary) were specified over the whole calculated domain.

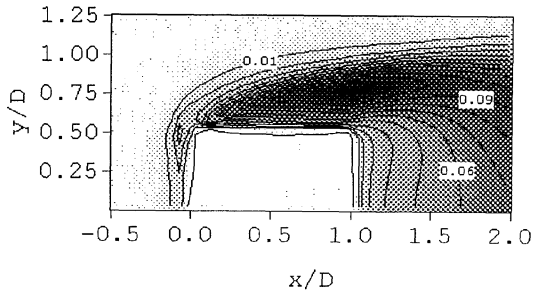

Figure 7(a). Distribution of k' around the column (Run 1)

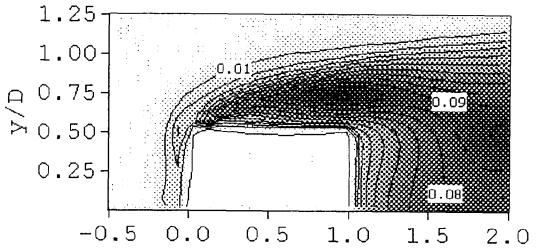

Figure 7(b). Distribution of k' around the column (Run 2)

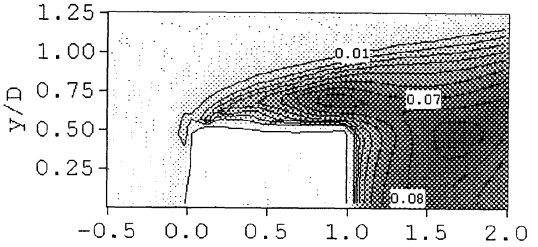

Figure 7(c). Distribution of k' around the column (Run 3)

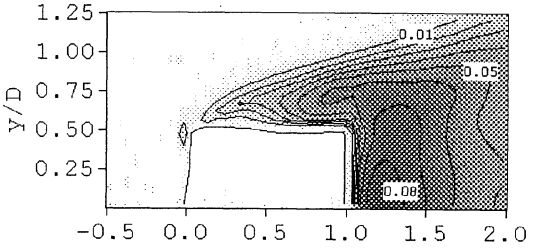

Figure 7(d). Distribution of k' around the column (Run 4)

Considerations of Calculated Results

In the calculated results for all Runs, the Karman vortex shedding was detected. The Strouhal number ($St = fD/U_0$) of the vortex shedding in all Runs was within the range of 0.144 to 0.146 and was about 11% larger than the

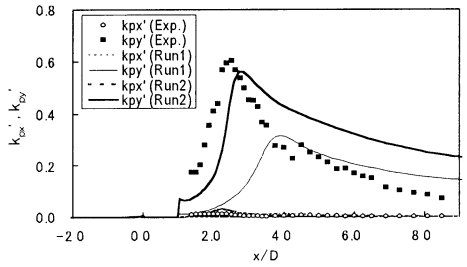

Figure 8 (a). k_{px}' and k_{py}' on x-axis (Run 1 ,2)

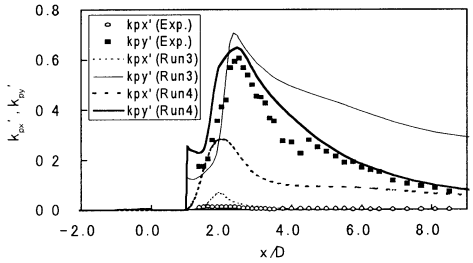

Figure 8 (b). k_{px}' and k_{py}' on x-axis (Run 3 ,4)

experimental value (St=0.13).

Figure 4 shows the distribution of the non-dimensional velocity component U/U_0 along x-axis. The length of the recirculation zone calculated in Run 1 is apparently too long and the recovery of the velocity at the downstream region of the recirculation zone is too slow. The recirculation zone in Run 2 is a little larger than the experimental one. On the other hand, Run 3 underpredict the length of the recirculation zone. Run 4 calculated precisely not only the length of the recirculation zone but also the whole distribution of the velocity.

The comparison of the non-dimensional turbulence energy k' ($=k/U_0^2$) is shown in Figure 5. The calculated values of k' in all models are considerably smaller than the experimental one. The similar discrepancies of k are indicated in the 2-D calculations with linear k-ε model by Bosch and Rodi (1998) and with RSM by Franke and Rodi (1993). Bosch and Rodi (1998) pointed out that the low-frequency modulation due to 3-D large-scale structure in the laboratory test can not be captured by the 2-D calculations, and thereby the calculated k' becomes much smaller than the experimental one.

The distribution of k' near the impinging region in Figure 5 is enlarged in Figure 6. Run 1 and 2 have large values of k' just before the impinging. The productions of k in Run 3 and 4 are suppressed. This figure demonstrates that the non-linear k-ε model with the effects of S and Ω can suppress the excessive production of k near the impinging region and the quadratic terms have no effect for the suppression.

Figure 7 (a) - (d) show the distributions of time-averaged turbulence energy k' near the column. The distributions in Run 1 and 2 are similar and have two peaks at the side and near the leading edge of the column. In Run 3 and 4, k around the column is smaller than that in Run 1 and 2.

Figure 8 (a) and (b) show the periodic part of the non-dimensional fluctuation energies in x-component, k_{px}, and in y-component, k_{py}, along x-axis. Every model overpredicts the

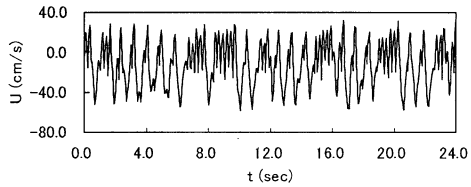

Figure 9. Temporal variation of U (Run 4, at x/D=6)

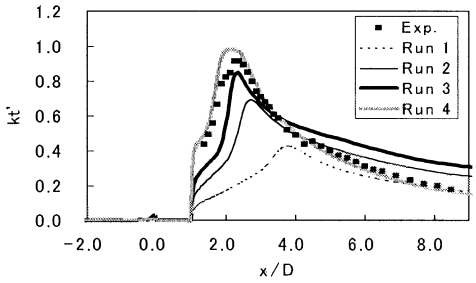

Figure 10. Total fluctuation energy on x-axis

peak value of k_{px}. Run 4 particularly gives very large values of k_{px} compared with the experiment. In the time trace of the stream-wise velocity in Run 4, the considerable deviation from periodicity was detected (Figure 9). It is supposed that the excessive production of k_{px} in Run 4 is caused by such irregularity of the velocity fluctuations. As for k_{py}, the peak value in Run 1 is very small and that in Run 2 is also a little smaller than the experimental one. Run 3 and 4 well predicted the peak value of k_{py} and the longitudinal distribution in Run 4 was in good agreement with the experimental one over the whole part of the plot.

Figure 10 shows the comparison of the non-dimensional total fluctuation energy k_t' (periodic part + turbulence part) along x-axis. The result in Run 1 is significantly smaller than the experimental one. Though the calculated peak value in Run 4 is slightly larger than the experimental one, Run 4 gave the most suitable distribution.

The transverse distributions of r.m.s. (root mean square) of the non-dimensional velocity variations (periodic part), U_{rms} and V_{rms} in Run 3 at two sections (x/D = 2.5 and x/D = 4.5) are shown in Figure 11 (a) and (b). In the section at x/D=2.5, V_{rms} has a peak on the center-line (y/D=0), and U_{rms} around y/D=0.7. The calculated results of the velocity variation in x/D=2.5 are in good agreement with the experiment ones. In x/D=4.5, the differences between the calculated and the experimental results both of U_{rm} and V_{rms} become larger compared with the results in x/D=2.5. It is pointed out through the examination of Figures 8, 10 and 11 that the model used in Run 3 could reproduce the periodic feature of the flow pattern qualitatively, though the model could not reproduce precisely the damping of the velocity variations toward the down-stream direction.

3-D CALCULATIONS OF FLOWS IN A OPEN CHANNEL

Computational Domain

The laboratory test was performed in the open channel with 15m (length) × 20cm (width). The averaged depth

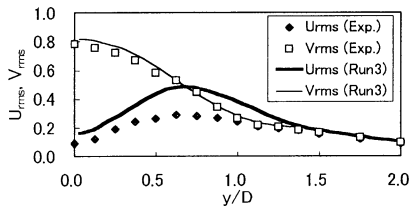

Figure 11 (a). Variations of U and V in transverse direction (r.m.s.) at x/D=2.5

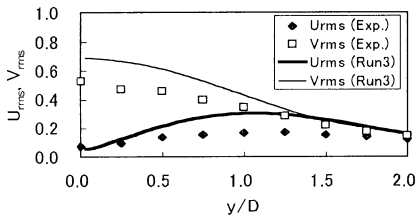

Figure 11 (b). Variations of U and V in transverse direction (r.m.s.) at x/D=4.5

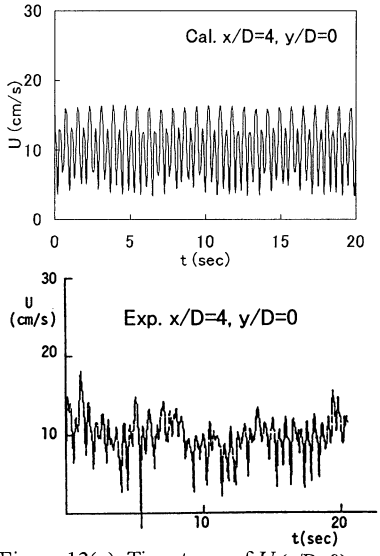

Figure 13(a). Time trace of U (y/D=0)

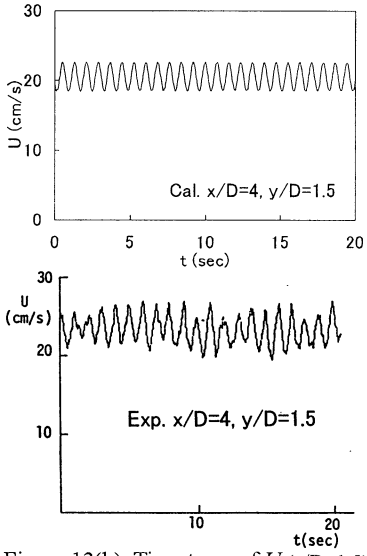

Figure 13(b). Time trace of U (y/D=1.5)

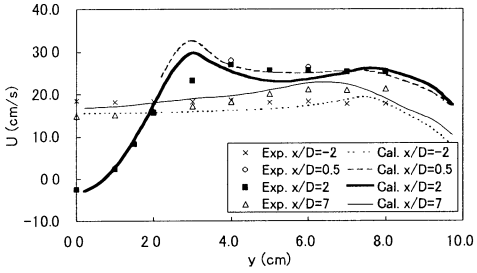

Figure 12. Time-mean velocity distributions

was h =1.14 cm (h/D=0.285) and the averaged velocity in the main flow at the upstream of a column was 18.18 cm/s (Re=8400, Fr=0.54). The square column with the side length of 4cm was placed on the center line of the channel.

The flow domain was divided into 10 (depth-wise direction) × 36 (transverse direction) × 120 (stream-wise direction) control volumes.

Numerical Method

The turbulence model in Run 3 was used in the calculation of the open channel flow. Numerical procedures were the same as those used to reproduce the Lyn's experiment except for the free surface treatment as summarized below.

The free surface elevation was calculated by solving the continuity equation integrated over the control volume of the surface layer. To consider the rapid attenuation of turbulent intensities in the depth-wise direction near the free surface, the eddy viscosity was multiplied by the following dumping function.

$$f_s = 1 - \exp\left(-B\frac{(h-y)\varepsilon_s}{k_s^{3/2}}\right), \quad (B=10) \tag{12}$$

where sub-s indicates the value at the surface layer. The turbulent dissipation rate at the surface layer was evaluated by the following formula proposed by Sugiyama et al. (1995) to calculate the secondary currents of 2nd kind.

$$\varepsilon_s = \frac{C_{\mu 0}^{3/4} k_s^{3/2}}{0.4\Delta y_s}, \quad (C_{\mu 0} = 0.09) \tag{13}$$

Considerations of Calculated Results

Figure 12 shows the time-averaged distributions of U in the laboratory test and the numerical simulation along 4 cross sections in the right part of x-axis. This figure indicates that the general time-averaged flow pattern around the column is simulated qualitatively.

Figure 13 (a), (b) show the comparison of temporal variations of U in the experimental and numerical results at two points ((x/D, y/D) = (4,0) and (4,1.5)). Good agreements can be seen in the periods of the variations in both the results at each point. The period at (x/D, y/D) = (4, 1.5) coincides with that of the Karman vortex shedding and the period at (x/D, y/D) = (4, 0) is the half of that. The Strouhal number of the Karman vortex is St = 0.253 and is about 11 % larger than the observed one (St = 0.231).

For the examination of effects of the depth to the 3-D flow structures, additional calculation was carried out under the depth of h/D=0.855, which is three times larger than the experimental one. Plan views of the instantaneous flow pattern at $z=h/2$ are shown in Figure 14 (a) and (b). The Karman vortex shedding is generated in both the figures. The recirculation zone at the downstream region of the column in Figure 14 (a) is larger than that in (b). Figure 15 (a) and (b) show the instantaneous flow pattern at the vertical section across the column in y-direction. Near both side-walls of the column, downward flows occur, on the other hand, flows away from the column are generated near the bed. Figure 16 (a) and (b) show the flow pattern at vertical section along x-axis. In upstream region of the column, a vortex in clock-wise direction is generated near the bed. The 3-D flow pattern shown in Figure 15 and 16 indicates the formation of the horses-shoe vortex.

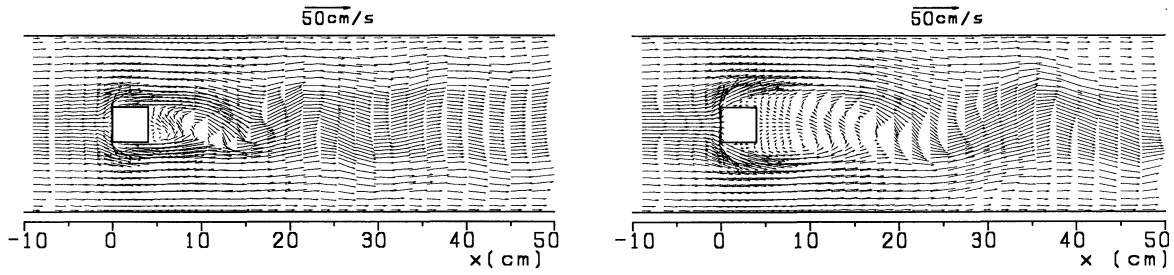

(a) h/D=0.285 (b) h/D=0.855

Figure 14. Plan view of flow patterns

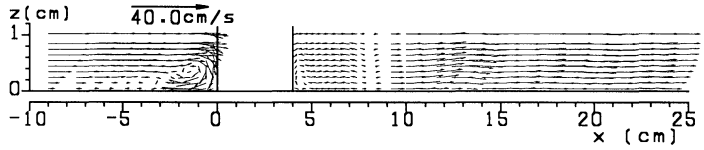

(a) h/D=0.285

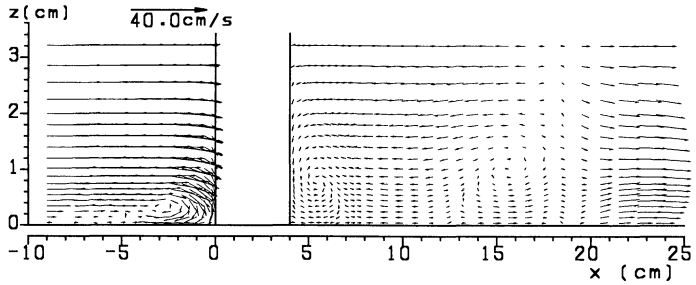

(b) h/D=0.855

Figure 15. Flow patterns in the vertical section along the x-axis

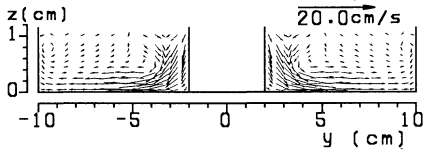

(a) h/D=0.285

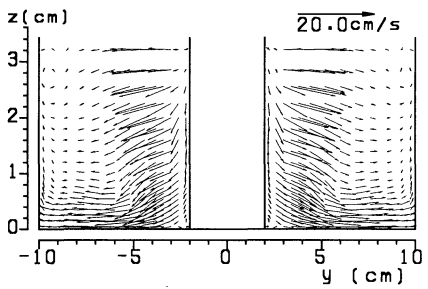

(b) h/D=0.855

Figure 16. Flow patterns in a cross section

CONCLUSIONS

The computational methods based on the non-linear k-ε models with the quadratic terms are applied to unsteady flows around a square column. The main results obtained in this study are summarized as follows:

3. 2-D calculations of the flow in a closed water section show that the standard k-ε model underpredicts the periodic motion considerably, and the non-linear k-ε model with the effects of the strain and the rotation parameters can suppress the excessive production of turbulence energy around a column.
4. 3-D unsteady flow patterns in open channels, i.e., the Karman vortex shedding and the horse-shoe vortex formation, were reproduced qualitatively by the 3-D calculation with the non-linear k-ε model.

REFERENCES

Bosch, G. and Rodi, W., 1998, "Simulation of Vortex Shedding past a Square Cylinder with Different Turbulence Models," *Int. J. Numerical Methods in Fluids*, Vol.28, pp.601-616.

Franke, R. and Rodi, W., 1993, "Calculation of Vortex Shedding past a Square Cylinder with Various Turbulence Models," *Turbulent Shear Flows* 8, Springer, pp.189-204.

Gatski, T. B. and Speziale, C. G., 1993, "On Explicit Algebraic Stress Models for Complex Turbulent Flows," *J. Fluid Mech.*, Vol.254, pp.59-78.

Hosoda, T., Kimura, I. and Muramoto, Y., 1997, "Vortex Formation Processes in Open Channel Flows with a Side Discharge by Using the Non-linear k-ε Model," *Proc. of 11th Symposium on Turbulent Shear Flows*, Grenoble, Vol.2, pp.19.1-19.6.

Kato, M. and Launder, B.E., 1993, "The Modeling of Turbulent Flow around Stationary and Vibrating Square Cylinders," *Proc. 9th Symposium on Turbulent Shear Flows*, Kyoto, Vol.1, pp.P10.4.1-10.4.6.

Lyn, D. A., 1992, "Vortex Shedding Past a Square Cylinder,"*ERCOFTAC Fluid Dynamics Database*, 43.

Lyn, D. A., Einav, W., Rodi, W. and Park, J.-H., 1995, "A Laser-Doppler Velocimetry Study of Ensemble-averaged Characteristics of the Turbulent near Wake of a Square Cylinder," *J. Fluid Mech.*, Vol.304, pp.285-319.

Pope,S.B., 1975, "A More General Effective Viscosity Hypothesis," *J. Fluid Mech.*, Vol.72, pp.331-340.

Sugiyama, H., Akiyama, M. and Matsubara, T., 1995, "Numerical Simulation of Compound Open Channel Flow on Turbulence with a Reynolds Stress Model," *J. of Hydraulic, Coastal and Environmental Eng.*, No.515/ II - 31, pp.55-65 (in Japanese).

Yoshizawa, A., (1984), "Statistical Analysis of the Deviation of the Reynolds Stress from its Eddy Viscosity Representation," Phys. Fluids, Vol.27, pp.1377-1387.